USE OF DIELECTRIC PADDING TO ELIMINATE LCF ARTIFACT IN CR-MREPT CONDUCTIVITY IMAGES

Journal:	*Magnetic Resonance in Medicine*
Manuscript ID	Draft
Wiley - Manuscript type:	Full Paper
Date Submitted by the Author:	n/a
Complete List of Authors:	Yildiz, Gulsah; Bilkent Universitesi, Electrical and Electronics Engineering Ider, Yusuf; Bilkent University, Electrical and Electronics Engineering
Research Type:	Artifacts < Technique Development < Technical Research, Contrast mechanisms (dynamic, etc.) < Contrast < Biophysics < Technical Research
Research Focus:	No specific tissue or organ focus
Note: The following files were submitted by the author for peer review, but cannot be converted to PDF. You must view these files (e.g. movies) online.	
SupportingInformationVideoS1.avi	

USE OF DIELECTRIC PADDING TO ELIMINATE LCF ARTIFACT IN CR-MREPT CONDUCTIVITY IMAGES

Gulsah Yildiz[1], Yusuf Ziya Ider[1,*]

[1] Department of Electrical and Electronics Engineering, Bilkent University, Ankara, Turkey

** Correspondence address:*

Yusuf Ziya Ider, PhD.

Department of Electrical and Electronics Engineering

Bilkent University

Ankara, Turkey

Phone: +90-312-290-2339, Fax: +90-312-266-4192

E-mail: ider@ee.bilkent.edu.tr

Grant support: This study was supported by TUBITAK 114E522 research grant.

Running head: Use of Dielectric Padding to Eliminate LCF Artifact in cr-MREPT Conductivity Images

Word Count: 4911

Abstract

Purpose

Convection-reaction-equation based magnetic resonance electrical properties tomography (cr-MREPT) provides conductivity images that are boundary artifact free and robust against noise. However, these images suffer from the Low Convective Field (LCF) artifact. We propose to use dielectric pads to alter the transmit magnetic field (H^+), shift the LCF region and eliminate the LCF artifact.

Methods

In computer simulations, pads with different parameters (electrical properties, pad thickness, pad height, arc angle, and thickness of the pad-object gap) are used. Two data sets with the pad located on the left or on the right of the object (phantom) are acquired, and the corresponding linear system of equations are simultaneously solved to get LCF artifact free conductivity images. In experimental studies, water pads and $BaTiO_3$ pads are used with agar-saline phantoms.

Results

A pad should have 180^o arc angle and the same height with the phantom for maximum benefit. Also, the closer the pad is to the phantom, the more pronounced is its effect. Increasing the pad thickness and/or the relative permittivity of the pad, increase the LCF shift while excessive amounts of these parameters cause errors in conductivity reconstructions because derivatives of Hz become non-negligible. Conductivity of the pad, on the other hand, has minimal effect on elimination of the LCF artifact.

Conclusions

Using the proposed technique, LCF artifact is removed and also the reconstructed conductivity values are improved. Thick water pads are proved to be better than the thin ones whereas high dielectric pads must be preferred as thin.

I. INTRODUCTION

Imaging the electrical properties (EPs: conductivity, permittivity) of tissues is beneficial in many respects. Conductivity imaging provides clinically important information due to conductivity differences among healthy tissues and also between healthy and malignant tissues [1,2]. Calculation of specific absorption rate [3] is another important application in high field MRI. Transcranial magnetic stimulation [4], hyperthermia treatment [5], and radiofrequency (RF) ablation [6] are examples of therapy monitoring applications requiring EP information.

The idea of calculating EPs at the Larmor frequency of an MR system has been proposed by Haacke in 1991 [7] and applied for the first time by Wen in 2003 [8]. Electrical properties tomography (EPT) has been reintroduced and extensively analyzed by Katscher in 2009 [3]. MREPT is based on the fact that EPs perturb the RF magnetic field and therefore they can be extracted from the information buried in the RF magnetic field. Haacke has developed the first formula for the relationship between admittivity ($\gamma = \sigma + i\omega\varepsilon_0\varepsilon_r$) and the RF magnetic field:

$$\gamma = \frac{\nabla^2 H^+}{i\omega\mu_0 H^+}, \tag{1}$$

where σ is the conductivity, ε_r is relative permittivity, ε_0 is free-space permittivity, ω is the Larmor frequency, and $H^+=(H_x+jH_y)/2$ is the complex left-hand rotating magnetic field, or in other words, the transmit magnetic field. Eq. (1) will be referred to as the standard MREPT (std-MREPT) method for the reconstruction of conductivity. This standard method is point-wise, prone to noise, and more importantly, it assumes locally constant EP values (the so called Local Homogeneity Assumption, LHA), which results in error at the tissue boundaries where EPs change abruptly.

Several studies to overcome the boundary artifact issue have been conducted. Gradient based electrical properties tomography uses a multi-channel transceiver RF coil and obtains the gradients of EPs, which are then integrated starting from a seed-point [9]. Contrast Source Inversion based EPT [10] tries to minimize the difference between the measured and the modelled H^+ data iteratively to find the EPs. Hafalir [11] has proposed the convection-reaction equation based MREPT (cr-MREPT) where the relation between EPs and the H^+ is modelled as a convection-reaction PDE. cr-MREPT is a global method, such that it finds the solution for all pixels simultaneously and considers the constraining effects of neighboring pixels on each other, so that it is more robust against noise. The cr-MREPT PDE is as follows:

$$\mathbf{F} \cdot \nabla u + \nabla^2 H^+ u - i\omega\mu_0 H^+ = 0 \tag{2}$$

where $u = 1/(\sigma + i\omega\varepsilon_0\varepsilon_r)$ is the unknown in cr-MREPT equation. In cylindrical phantoms where there is no change in EPs along z-direction, derivative of “u” in z-direction becomes zero. In such cases, the cr-MREPT PDE will simplify to its 2D form, where

$$\overline{\nabla} u = \begin{bmatrix} \frac{\partial u}{\partial x} \\ \frac{\partial u}{\partial y} \end{bmatrix} \text{ and } \mathbf{F} = \begin{bmatrix} F_x \\ F_y \end{bmatrix} = \begin{bmatrix} \frac{\partial H^+}{\partial x} - i\frac{\partial H^+}{\partial y} + \frac{1}{2}\frac{\partial H_z}{\partial z} \\ i\frac{\partial H^+}{\partial x} + \frac{\partial H^+}{\partial y} + \frac{i}{2}\frac{\partial H_z}{\partial z} \end{bmatrix} \tag{3}$$

Note that $F_y = iF_x$ and $\mathbf{F}$ is referred to as the convective field.

H_z cannot be measured in MRI, and using a transverse RF excitation field with a volume birdcage coil, in the center slices, derivatives of H_z are significantly smaller than the derivatives of H^+ and therefore they are neglected by many investigators. The convective field is then calculated as

$$\boldsymbol{F} = \begin{bmatrix} F_x \\ F_y \end{bmatrix} = \begin{bmatrix} \frac{\partial H^+}{\partial x} - i\frac{\partial H^+}{\partial y} \\ i\frac{\partial H^+}{\partial x} + \frac{\partial H^+}{\partial y} \end{bmatrix} \tag{4}$$

When $|\mathbf{F}|$ is very low, the solution for *u* displays artifacts. This region is called the Low Convective Field (LCF) region and the resulting distortion is called the LCF artifact. While being a spot-like artifact in simulation studies, the effect of LCF is increased due to noise in experimental data, resulting in a disturbed region, generally in the center of the object. gEPT also suffers from a similar artifact, as mentioned as a “global bias” in [12]. Also, it is observed in CSI-based methods that low E field regions, which are identical with the LCF regions, result in artifacts [10,13]. Hafalir proposed a double-excitation method by cutting a portion of the phantom and repeating the data collection. Although it eliminates the LCF artifact, it would be impractical in a real life application. Another multi-excitation method is presented by Ariturk where a multichannel TEM array is used to obtain different H^+ fields with shifted LCF regions [14]. This method however is demanding on the RF amplifiers and requires a multi-transmit coil and system. Gurler proposed a phase-based MREPT, which uses the phase data only and suffers less from LCF artifact [15]. In general phase-based methods give high contrast conductivity images, but they fail to give the correct values as they assume low B_1^+ magnitude gradients [16, 17].

Regularization, based on introducing an artificial diffusion term in the cr-MREPT PDE, has been proposed to mitigate LCF artifacts [18,19]. Determination of the value the regularization parameter (the diffusion constant) is still a major issue in such methods because one has to compromise spatial resolution (concomitant with blurring) with elimination of the LCF artifact. Although one may experience complete elimination of the LCF artifact in some numerical simulation cases, it is our experience that LCF artifact reappears when noise is added to the simulated data or when actual noisy experimental data are used [19].

High dielectric pads are generally being used in high field MRI for shimming purposes [20-23] while padding is also applied to improve electrical properties estimation [13]. $CaTiO_3$ and $BaTiO_3$ are the most widely used materials for padding due to their high dielectric constants. In the literature, the powder form of these materials are mixed with water to obtain slurries, while a bead-water mixture can also be used [24]. In a preliminary study [25], we have shown that using high dielectric pads, one can shift the LCF region. Furthermore, it is shown that if two data sets with non-overlapping LCF regions are simultaneously solved, LCF artifacts can be eliminated in conductivity maps.

In this paper, we investigate the double-excitation method using dielectric pads to eliminate the LCF artifact in cr-MREPT conductivity maps. First, the effect of a dielectric pad on the H^+ field in the object is studied by simulations, and then padding is applied both in simulation and experimental studies for cr-MREPT. Two cases, where the LCF regions do not overlap (by use of pad in various locations), are solved simultaneously to reconstruct conductivity using cr-MREPT method. Results for different pads are simulated and the optimum pad structure for MREPT is determined. Phantom experiments with BaTiO3 slurry pad and water pad are also conducted and the reconstructed conductivity images are compared.

II. METHODS

A. Simulation Methods

Simulations have been conducted in COMSOL Multiphysics 5.2a (COMSOL AB, Stockholm, Sweden), using the frequency domain study in Radio Frequency Module. Quadrature birdcage coil (QBC) model is used for transmission. The coil is 24 cm in height, 14.5 cm in radius, and has 16 rungs. The QBC coil is excited in the quadrature volume transmit mode where two ports which are spatially 90^o apart are driven by voltage sources (100V rms) with 90^o phase offset with respect to each other [26]. Electromagnetic study is performed at 127.7MHz, the nominal frequency of a 3T MR system. Calculated H^+ is exported with 1 mm resolution.

Simulation Phantoms and pads

A cylindrical phantom (height=15 cm, radius=6 cm) with two anomalies is designed (Figure 1a). Small anomaly has σ=1 S/m and large anomaly has σ=1.5 S/m while background has σ=0.5 S/m. The whole phantom has ε_r=80 and μ_r=1 (relative permeability). For -0.5 cm<z<0.5 cm, the mesh size is less than 1.75 mm and the data are taken from the z=0 slice. Mesh is at most 3 mm in the rest of the phantom (Figure 1b). In some studies, the anomalies are removed and a homogeneous phantom with ε_r=80 and σ=0.5 S/m is obtained. Figure 1d displays a 3D head model [26], the conductivity properties of which are shown in Figure 1f. Mesh is arranged similar to the cylindrical phantom (Figure 1e) and the data are taken from the z=0 slice.

In Figures 1a,b an example pad with 1 cm thickness and 2 mm gap is shown, where it lies along the full height of the object. When pure water pads are simulated, the corresponding material properties are ε_r=80 and σ=0 S/m. The 150, 220 and 290 relative permittivity values are meant to represent pads made by different ratios of $BaTiO_3$ and water. Pad in the head model simulation is shown in Figure 1d. Head pad is designed to have a shape which would be expected in a real experiment.

B. Experimental methods

1) Experimental Phantom Preparation

Cylindrical experimental phantom (height=17 cm, radius=12.5 cm) is used. Background of the phantom is prepared using an agar/saline gel (20 g/L agar, 2 g/L NaCl, 1.5 g/L $CuSO_4$) and the higher conductive regions are prepared using a saline solution (20 g/L agar, 6 g/L NaCl, 1.5 g/L $CuSO_4$). Background is expected to have app. 0.5 S/m conductivity where the anomaly regions are expected to have app. 1 S/m [27].

2) Pad Preparation

Two kinds of material for padding are considered: water and $BaTiO_3$ slurry. Two different $BaTiO_3$ powders from different vendors (MERCK and Entekno) are used, two slurries with $BaTiO_3$/water weight ratio of 2/1 are prepared. The slurries are collected into polyethylene bags which are hot-sealed (Figure 1g).

Std-MREPT is used to measure the dielectric constant and the conductivity of the resulting slurries. As the $BaTiO_3$ slurry (suspension) is not homogenous and also some of the $BatiO_3$ precipitates in time, std-MREPT images are noisy and the obtained H^+ needs to be highly filtered. A 5x5x5 median filter and 5x5x5 Gaussian filter with s.d. of 5 are applied. For two different $BaTiO_3$ slurries, dielectric constant and conductivity are obtained as: for Merck, $\varepsilon_r = 187.6 \pm 42.5$ (s.d.) and $\sigma = 0.05$ S/m $\pm$ 0.8 (s.d.); for Entekno, $\varepsilon_r = 214.1 \pm 18.9$ (s.d.) and $\sigma = 1.96$ S/m $\pm$ 0.45 (s.d.).

3) Experiment Setup and Registration of Datasets

In general, three consecutive data sets are acquired: without pad (NP-no pad), pad on the left side (LP) and pad on the right side (RP). One important point is that the object should not move between the successive experiments. A Styrofoam dock is used to prevent motion during the experiment (Figure 1h). However, while placing and stabilizing the pad, the phantom may still move. To spatially match the datasets, “Genetic Algorithm” (GA) method is used as the optimization tool for registration of the images onto each other [28].

4) MR Sequences

Experiments are performed using Siemens Tim Trio 3T Scanner (Erlangen, Germany). We use double angle (DA) method [29] for B_1^+ (or equivalently H^+) magnitude mapping and bSSFP sequence to obtain the B_1^+ phase. Body QBC is used for transmit and Phased-Array is used for receive in the two gradient-echo sequences which are used for DA. Sequence parameters are as follows: FoV=170mm, voxel size=1.3mmx1.3mmx3mm, flip angles=60/120, TE/TR=5/1500ms, NEX=4, total duration for DA=26 min.

bSSFP is used due to its speed and high SNR features, also it does not have the additional phase component due to eddy-currents, which makes it a better option than a spin-echo sequence. Body QBC is used both for transmit and receive. Transcieve Phase Approximation (TPA) is used, and the transmit phase is taken as half of the transcieve phase [3]. bSSFP parameters are: FoV=170mm, voxel size=1.3mmx1.3mmx3mm, flip angle=40, TE/TR=2.23/4.46ms, NEX=32, duration=20 sec.

C. Numerical methods

Numerical methods are implemented in MATLAB (Mathworks, Natick, MA, USA). H^+, either from the simulation environment or from MRI, is obtained on a regular grid and is interpolated into a triangular mesh. For experiments, diffusion filter, which corresponds to a Gaussian filter with s.d. of 1.7 mm, is used for denoising. Gradients and Laplacian are calculated using the method proposed by Fernandez [30].

The cr-MREPT PDE is discretized to build a linear system of equations as explained in [11]. At boundaries we use Dirichlet boundary condition, and boundary values are set to σ=0.5 S/m and ε_r=80. Even if the given boundary values are not exactly correct, the values converge to the correct ones within couple of pixels towards the inside of the object. While finding "u", backslash operator of MATLAB is used, which uses the Minimum Norm Least-Squares approach. When the two data sets, or more, are being solved simultaneously, the system of equations are concatenated and again the backslash operator is used.

III. RESULTS

A. Simulation results

1. Effect of Pad on the RF magnetic field H^+

Simulations are conducted to understand and visualize the effects of pads on the object. The primary rotating electromagnetic field created by the QBC results in current flow within both the pad and the object. The homogeneous phantom together with a (left) pad which has uniform EP of ε_r=80 and σ =0 S/m are simulated, and the current distribution in the pad is displayed in Figure 2a. Since H^+ is a (left-hand) rotating field, the current distribution also rotates. At different phase instants, current flow direction and intensity change throughout the pad as shown in Figures 2a-d. Also an animation showing the rotating current distribution is given by the Supporting Information Video S1.

One can view the current in the pad as one of the sources which generate the H^+ field in the object. To exhibit its contribution, i.e. the effect of the pad, three simulations are conducted in series:

i) The QBC is excited but a pad is not introduced. The magnetic field generated in the object, i.e. the field caused by the coil, H_C^+, is given in Figure 2e.

ii) The QBC is excited and also a pad is placed on the left-hand-side of the object. The magnetic field for this simulation, called H_T^+ (T for total), is given in Figure 2g. The current distribution induced in the pad is saved to disc.

iii) The QBC is not excited (the driving voltage sources are killed) and the pad is replaced by a volume current source identical to the current distribution saved in the previous step. The field in the object obtained in this case, i.e. the contribution of the pad to the object's magnetic field, H_P^+, is shown in Figure 2f.

As shown in Figure 2h it is found that $H_C^+ + H_P^+ \approx H_T^+$. The extra magnetic field (H_P^+) and the primary magnetic field (H_C^+) are in phase; therefore, the magnetic field close to the high dielectric pad becomes higher in magnitude.

The same simulations are repeated with a pad that has uniform EP of ε_r=150 and σ =1 S/m. For this case, the same magnetic fields as explained above are shown in Figures 2i-l and it is observed that H_T^+ has lower magnitude. This is due to the fact that in this case, the pad has conduction currents due to σ as well as dielectric currents due to ε_r. The conduction current and the field generated by it are out of phase with those of ε_r and therefore the effect of σ subtracts from the field generated by the coil.

2. Effect of Pad Parameters on LCF Shift

The amount of the LCF shift in the presence of a pad depends in general on the amount of current flowing inside the pad. The parameters that effect the amount of current are the EPs of the pad material, thickness of the pad (PT), angle of the arc that the pad subtends (PA), the height of the pad (PH), and the gap thickness (GT).

Simulation results for the NP case are shown in Figures 3a-c, where the convective field can be seen. The LCF region is almost at the center and the location of the minimum value of the convective field is shown on Figure 3c. A LP (PT=2 cm, GT= 2mm, σ=0 S/m) is placed and the dielectric constant of the pad is varied. The convective fields are obtained and the locations of the corresponding convective field minimums are displayed in Figure 3d. The direction of the LCF shift is towards one end of the pad; moreover, for a fixed pad location changing the pad's dielectric constant, thickness, height and the gap thickness does not alter the direction of the shift but only the amount of it. However, looking to Figure 3e, this is not the case for changing the pad's conductivity. Keeping other parameters fixed and varying the conductivity of the pad, one can observe that the locations of the convective field minimums shift almost on an arc centered on the NP minimum location rather than a straight trajectory. A similar difference was observable with the H^+ magnitudes given in Figure 2, such that the inclination of H^+ is also different between pure-dielectric and conductive-dielectric pads.

Figures 4a-d display the dependence of the amount of LCF shift on the thickness of the pad, the amount of gap thickness, and the value of the dielectric constant of the pad. LCF shift is calculated as the Euclidean distance between the locations of the convective field minimums of NP and LP. No-gap pads (gap thickness is 0 mm) give rather high shifts than pads with non-zero gap. This is due to the fact that a very low dielectric medium (air) is introduced between the pad and the object when there is a non-zero gap and consequently the effect of the pad is significantly reduced. However, in practice since a gap may be unavoidable, it is more interesting to observe the results of a non-zero gap, and even up to 30 mm shifts are possible with such pads. It can be observed that, for a PT=1 cm pad and GT=2 mm, 3 to 7 mm shifts are possible as ε_r is varied from 80 to 290. Similar amount of shifts is achieved with a 2 cm thick pad even when GT is 8 mm. In general, looking through the different PT results, if GT is needed to be increased, then the PT can be increased to balance the amount of the shift. Considering the effect of ε_r, the amount of the shift increases with increasing dielectric constant, irrespective of the values of the other parameters. Dependence of LCF shift to ε_r seems to be linear with PT=1-2 cm pads; but the incremental effect is more pronounced as ε_r is increased for the cases of PT=3-4 cm pads. LCF shift dependence on 1/GT, on the other hand, is not linear, in the sense that, doubling GT will not cause the amount of the shift to be halved. Increasing PT or ε_r both act to increase the LCF shift and therefore they can be used as a substitute for each other. For example, a pad with PT=2 cm and ε_r=290, and another pad with PT=4 cm and ε_r= 150, both cause about 15 mm of LCF shift.

Another set of simulations is conducted to clarify the effect of the angle that the pad subtends. PT=3 cm pad with ε_r=150 and GT=2 mm, is wrapped around the phantom with increments of 45^0 until it reaches the full coverage. The amount of the LCF shift with respect to PA can be seen in Figure 4e. Until 180^0 the amount of the shift increases, whereas after 180^0 the effect reverses and the amount of the shift decreases since the effects enforced from opposite sides begin to cancel. As 180^0 of arc angle gives the highest shift, all the pads in this study have 180^0 of arc angle unless otherwise stated.

The height of the pad is also another important factor. Keeping the center of the pad fixed at z=0 (PT=3 cm, GT=2 mm, ε_r=150), the height is varied from 2.5 cm to 20 cm with 2.5 cm steps. Although the results are acquired from the center slice, the amount of the LCF shift is still influenced by PH; in fact, with 2.5 cm high pad, no shifts are observed. The relation between PH and the LCF shift amount is displayed in Figure 4f. Until 15 cm, which is also the height of the object itself, the relation seems to be almost linear. When PH exceeds the height of the object, increments in the shifts get smaller, though the LCF still shifts further.

3. Effect of Pad Parameters on Combined Conductivity Maps

The main purpose of this study is to determine whether, by using padding, the LCF artifacts in the conductivity maps are eliminated (or reduced) and the conductivity values are more correct. To monitor the effect of the pad parameters on the final conductivity map, reconstructions for individual pad cases are made separately and also for when the data are combined as previously explained.

For conductivity reconstructions, the first phantom model with 2 anomaly regions is used. Figure 5 displays H^+ magnitude, convective field, and conductivity maps for left pad with ε_r=290, NP, and right pad with ε_r=290 (pads have PT=1 cm and GT=2 mm and σ=0 S/m). Dielectric constant of 290 is a relatively high value and the highest that we analyzed, and it succeeds to separate LCF regions (LCF artifacts) from each other to a large extend. Seeing the behavior of LCF artifacts in Figures 5c,f,i and examining them throughout the study, LCF artifacts do not show themselves in a predetermined shape, but instead change their pattern depending on whether the LCF is in or out of an anomaly or whether it coincides with the boundary of an anomaly; the LCF artifact may have patterns like a single dip, a single peak, or both, with the effect fading within couple of pixels or within dozens.

As it is proposed, different data sets are combined to get rid of the LCF artifact: left pad and without pad (LP+NP), right pad and without pad (RP+NP), and left pad and right pad (LP+RP). Figures 5j-l display the corresponding combined conductivity results and also the conductivity profiles (on the line given in Figure 5m) is plotted in Figure 5m. LP+RP combination gives better accuracy and it effectively eliminates the LCF artifact.

A similar simulation result is given in Supporting Information Figure S1 for the same pad but with ε_r=80. Combined conductivity map for this simulation fails to fully eliminate the artifact while still being more accurate than NP conductivity map. Looking at the LCF artifacts in with and without pad cases, it can be seen that they are not sufficiently far away from each other (the LCF regions overlap) and therefore the artifact is not eliminated completely.

LP+RP combination conductivity results for pads with ε_r=[80, 150, 220, 290], σ=[0 S/m, 1 S/m] and PT= [1 cm, 3 cm] are provided in Figure 6 and the percent L^2-errors are also given below the corresponding images (Percent L^2-error is calculated excluding the anomaly boundaries). Having the lowest dielectric constant of studied EPs, ε_r=80 pad provides more accuracy if it is made thicker as opposed to higher dielectric pads. For example using a PT=3 cm and ε_r=290 pad gives very poor accuracy, whereas a PT=3 cm and ε_r=80 pad gives the highest accuracy among the studied pads. Adding σ=1 S/m to pads, it affects the results minimally when the pad is thin, while it increases the error rate with thicker pads.

The fact that the combined conductivity values are highly distorted with thick high dielectric pads is not what we had expected (see for example in Figures 6 j,k,n,p). Moreover, it is also unexpected to see that the individual (not combined) conductivity values are also poor in accuracy also in regions other than the LCF (Figures 5c,f,i). It is suspected that neglecting the derivatives of H_Z in Eq. (3) may be the reason. To examine the effect of this assumption, reconstruction process is repeated with the H_Z terms included. Supporting Information Figure S2 shows the individual and combined conductivity images, where a PT=1 cm ε_r=290 σ=0 S/m pad is used. Comparing the individual conductivity images with the ones in Figure 5, one can conclude that neglecting the derivatives of H_Z, in fact, causes errors which are even higher with high dielectric pads. With thinner or lower ε_r pads, combined conductivity maps are less erroneous, such that combining the data sets overcomes the issues formed by neglecting the H_Z derivatives; however, with thicker and higher ε_r pads, derivatives of H_Z become significant and conductivity maps are incorrect. Considering Figure 6 again, for ε_r=220 or ε_r=290, thin pads with PT=1 cm are suitable, but when ε_r= 80, a thick pad with PT = 3 cm can be used.

Simulation results using the head simulation model and a pad with PT=2 cm, GT=2 mm, ε_r=220 and σ=0 S/m is given in Figure 7. Individual and combined conductivity reconstructions, and their profiles along the introduced white line are presented. With this head phantom simulation model, the LCF artifacts in both the LP and RP cases are considerably shifted. The conductivity maps obtained with (LP+RP) and (LP+NP) combinations are satisfactory from the point of view of reduced LCF and accuracy of the conductivity values.

B. Experimental results

For the two anomaly experimental phantom the bSSFP magnitude images are shown in Figures 8a-c for the NP, left water pad and right water pad cases. Pad is approximately 2.5 cm and is approximately 2 mm away from the phantom. Expected conductivity map, Figure 8d, is formed using the bSSFP magnitude image. H^+ magnitude images for experiments NP, LP and RP are given in Figures 8e-g. Similar to what has been observed in simulations, the inclination of the H^+ field magnitude is towards the pad. Individual (uncombined) conductivity maps, Figures 8i-k, have severe LCF artifacts. Figure 8h displays std-MREPT result for NP. Figure 8l displays the combined (LP+RP) conductivity map. Conductivity profiles (on the white line given in Figure 8d) of NP and LP+RP are plotted in Figure 8m. Combined result does not suffer from the LCF artifact and has more accurate results than NP.

Several other experimental results are given in Figure 9. Conductivity maps for NP and (LP+RP) are given for each experiment. Also, the reconstructed conductivity profiles on the indicated white lines are shown. Results using a thin water pad (PT=1.5 cm max) are given in Figures 9a-d. Even though this is a thin pad and its dielectric constant is not as high as a $BaTiO_3$ slurry, LCF artifact is eliminated with (LP+RP) pad combination. However, since this pad is not very successful at shifting the LCF region the conductivity values of the combination result are not accurate. Non-conductive BaTiO3 slurry pad (PT=3 cm max) experiment results are given in Figures 9e-h. (LP+RP) combined conductivity map is free from the LCF artifact and also more accurate than NP. Figures 9i-l shows results for a somewhat different phantom in which large and small anomalies are present, and for this case conductive BaTiO3 slurry pad is used. The big anomaly region's conductivity is found just as expected whereas the small anomalies are less accurate but still they have better accuracy than in the NP reconstruction. Besides, the LCF artifact is eliminated. Even though the simulation results with conductive pads are less accurate than the non-conductive ones, when the experimental results are considered, there aren't major differences between them probably due to the presence of experimental noise and also the filters that we have used to combat the noise. The bSSFP magnitude and H^+ magnitude images for NP, LP and RP pad situations for the experiments described in Figure 9, are given in Supporting Information Figure S3.

In additional experiments, we have repeated the bSSFP sequence 32 times in order to achieve more averaging and thus more SNR in the phase of H^+. Results of these experiments, in which a non-conductive BaTiO3 slurry pad is used (PT=3 cm max), are shown in Figure 10. Again, LP+RP combinations yield LCF artifact free images. These images are less noisy, compared to the images in Figure 9, due to the higher SNR of the data despite the fact that we have used higher cut-off low pass filters for these cases (Gaussian filter with s.d. of 1 mm).

IV. DISCUSSION AND CONCLUSIONS

Throughout this paper, padding technique has been proposed to improve the cr-MREPT method. Both simulation and experimental results show that the LCF artifact on conductivity maps can be removed with the padding method while also improving the accuracy of the conductivity values. We have also provided information about the mechanism of pad action which may be useful for B_1 shimming studies.

Though the amount of the LCF shift is important so that the LCF regions do not overlap, excessive amount of shift is undesired. This is due to the fact that we neglect the derivatives of the H_Z field and although they are negligible in most of the birdcage studies [3], they become significant with the use of high dielectric pads. The larger the effect of the pad, the more critical H_Z becomes and therefore the error due to neglecting H_Z derivatives in Eq. (3) increases. Therefore, if high dielectric pads (e.g. $BaTiO_3$ slurry) are used they must be prepared as thin, or using a thick water pad may be preferred.

An important issue is the time constraint for data acquisition. For each of the experimental phantoms covered in this work, three different sets of data have been acquired and different pairs are used for the final image reconstruction. However, in general it is observed that, left and right pad combinations give the best results as LCF regions tend to be further away with these pad cases.

Regularization methods have been proposed by several investigators in order to reduce noise effects and/or algorithm-caused spurious oscillations [31,32]. Also as mentioned in the introduction, artificial diffusion, which is another way of regularization, is proposed for reduction of the LCF artifact [18,19]. In this work we have not utilized any regularization method because we wanted to concentrate on the performance and limitations of the padding technique. Future work may cover combined use of regularization and padding as well as comparison of the two approaches.

Acknowledgement

This study was supported by TUBITAK 114E522 research grant. Experimental data were acquired using the facilities of UMRAM, Bilkent University, Ankara.

References

1. Joines W, Zhang Y, Li C, Jirtle R. The measured electrical properties of normal and malignant human tissues from 50 to 900 MHz. *Med Phys*. 1994;21(4):547-550. doi:10.1118/1.597312.
2. Surowiec A, Stuchly S, Barr J, Swarup A. Dielectric properties of breast carcinoma and the surrounding tissues. *IEEE Transactions on Biomedical Engineering*. 1988;35(4):257-263. doi:10.1109/10.1374.
3. Katscher U, Voigt T, Findeklee C, Vernickel P, Nehrke K, Dossel O. Determination of Electric Conductivity and Local SAR Via B1 Mapping. *IEEE Trans Med Imaging*. 2009;28(9):1365-1374. doi:10.1109/tmi.2009.2015757.
4. Salinas F, Lancaster J, Fox P. 3D modeling of the total electric field induced by transcranial magnetic stimulation using the boundary element method. *Phys Med Biol*. 2009;54(12):3631-3647. doi:10.1088/0031-9155/54/12/002.
5. Balidemaj E, Kok H, Schooneveldt G et al. Hyperthermia treatment planning for cervical cancer patients based on electrical conductivity tissue properties acquired in vivo with EPT at 3 T MRI. *International Journal of Hyperthermia*. 2016;32(5):558-568. doi:10.3109/02656736.2015.1129440.
6. Kwon O, Chauhan M, Kim H et al. Fast conductivity imaging in magnetic resonance electrical impedance tomography (MREIT) for RF ablation monitoring. *International Journal of Hyperthermia*. 2014;30(7):447-455. doi:10.3109/02656736.2014.966337.
7. Haacke E, Petropoulos L, Nilges E, Wu D. Extraction of conductivity and permittivity using magnetic resonance imaging. *Phys Med Biol*. 1991;36(6):723-734. doi:10.1088/0031-9155/36/6/002.
8. Wen H. Noninvasive quantitative mapping of conductivity and dielectric distributions using RF wave propagation effects in high-field MRI. Proc. SPIE 5030, Medical Imaging: Physics of Medical Imaging 2003. doi: 10.1117/12.480000.
9. Liu J, Zhang X, Schmitter S, Van de Moortele P, He B. Gradient-based electrical properties tomography (gEPT): A robust method for mapping electrical properties of biological tissues in vivo using magnetic resonance imaging. *Magn Reson Med*. 2014;74(3):634-646. doi:10.1002/mrm.25434.
10. Balidemaj E, van den Berg C, Trinks J, van Lier A, Nederveen A, Stalpers L, Crezee H, Remis R. CSI-EPT: A Contrast Source Inversion Approach for Improved MRI-Based Electric Properties Tomography. *IEEE Trans Med Imaging* 2015;34:1788-1796. doi: 10.1109/tmi.2015.2404944.
11. Hafalir F, Oran O, Gurler N, Ider Y. Convection-Reaction Equation Based Magnetic Resonance Electrical Properties Tomography (cr-MREPT). *IEEE Trans Med Imaging*. 2014;33(3):777-793. doi:10.1109/tmi.2013.2296715.
12. Liu J, Wang Y, Katscher U, He B. Electrical Properties Tomography Based on B_1 Maps in MRI: Principles, Applications, and Challenges. *IEEE Transactions on Biomedical Engineering*. 2017;64(11):2515-2530. doi:10.1109/tbme.2017.2725140.
13. Schmidt R, Webb A. A new approach for electrical properties estimation using a global integral equation and improvements using high permittivity materials. *Journal of Magnetic Resonance*. 2016;262:8-14. doi:10.1016/j.jmr.2015.11.002.

14. Ariturk G, Ider Y. Optimal multichannel transmission for improved cr-MREPT. *Physics in Medicine & Biology*. 2018;63(4):045001. doi:10.1088/1361-6560/aaa732.
15. Gurler N, Ider Y. Gradient-based electrical conductivity imaging using MR phase. *Magn Reson Med*. 2016;77(1):137-150. doi:10.1002/mrm.26097.
16. van Lier A, Brunner D, Pruessmann K et al. B 1+ Phase mapping at 7 T and its application for in vivo electrical conductivity mapping. *Magn Reson Med*. 2011;67(2):552-561. doi:10.1002/mrm.22995.
17. Voigt T, Katscher U, Doessel O. Quantitative conductivity and permittivity imaging of the human brain using electric properties tomography. *Magn Reson Med*. 2011;66(2):456-466. doi:10.1002/mrm.22832.
18. Li C, Yu W, Huang S. An MR-Based Viscosity-Type Regularization Method for Electrical Property Tomography. *Tomography*. 2017;3(1):50-59. doi:10.18383/j.tom.2016.00283.
19. Ider YZ, Boga C. Spatial resolution of Full cr-MREPT: 2D and 3D evaluation. In Proceedings of the 26th Annual Meeting ISMRM, Paris, France, 2018; 5098.
20. Yang Q, Wang J, Wang J, Collins C, Wang C, Smith M. Reducing SAR and enhancing cerebral signal-to-noise ratio with high permittivity padding at 3 T. *Magn Reson Med*. 2010;65(2):358-362. doi:10.1002/mrm.22695.
21. Yang Q, Herse Z, Ketterman M et al. Enhancement of RF field by high dielectric constant pad at 3T: cervical spine imaging. In Proceedings of the 19th Annual Meeting of ISMRM, Montreal, Canada, 2011, p. 621.
22. Schmitt M, Feiweier T, Horger W, Krueger G, Schoen L, Lazar R, Kie- fer B. Improved uniformity of RF-distribution in clinical whole body- imaging at 3T by means of dielectric pads. In Proceedings of the 12th Annual Meeting of ISMRM, Kyoto, Japan, 2004, p. 197.
23. Haines K, Smith N, Webb A. New high dielectric constant materials for tailoring the B 1 + distribution at high magnetic fields. *Journal of Magnetic Resonance*. 2010;203(2):323-327. doi:10.1016/j.jmr.2010.01.003.
24. Luo W, Lanagan M, Sica C et al. Permittivity and performance of dielectric pads with sintered ceramic beads in MRI: early experiments and simulations at 3 T. *Magn Reson Med*. 2012;70(1):269-275. doi:10.1002/mrm.24433.
25. Yildiz G, Ariturk G, Ider YZ. Use of Padding to Eliminate the LCF Artifact in Conductivity Maps Obtained by cr-MREPT. In Proceedings of the 25th Annual Meeting ISMRM, Honolulu, USA, 2017; 1949.
26. Gurler N, Ider Y. Numerical methods and software tools for simulation, design, and resonant mode analysis of radio frequency birdcage coils used in MRI. *Concepts in Magnetic Resonance Part B: Magnetic Resonance Engineering*. 2015;45(1):13-32. doi:10.1002/cmr.b.21279.
27. Iwase E. Electrıcal Conductıvıtıes Of The Salt Solutıons Contaınıng Agar. *Bull Chem Soc Jpn*. 1927;2(3):61-65. doi:10.1246/bcsj.2.61.
28. Meskine F, Mezouar M, Taleb N. A Rigid Image Registration Based on the Nonsubsampled Contourlet Transform and Genetic Algorithms. *Sensors*. 2010;10(9):8553-8571. doi:10.3390/s100908553.
29. Stollberger R, Wach P. Imaging of the active B1 field in vivo. *Magn Reson Med.* 1996;35:246-251. doi: 10.1002/mrm.1910350217.
30. Fernandez FA, Kulas L. A simple finite difference approach using unstructured meshes from FEM mesh generators. In Proceedings of IEEE15th International Conference on Microwaves, Radar and Wireless Communications, Warsaw, Poland, 2004; p. 585–588.
31. Ropella K, Noll D. A regularized, model-based approach to phase-based conductivity mapping using MRI. *Magn Reson Med.* 2016;78(5):2011-2021. doi:10.1002/mrm.26590.
32. Wang Y, Van de Moortele P, He B. CONtrast Conformed Electrical Properties Tomography (CONCEPT) based on Multi-channel Transmission. In Proceedings of the 25th Annual Meeting ISMRM, Honolulu, HI. 2017; 3640.

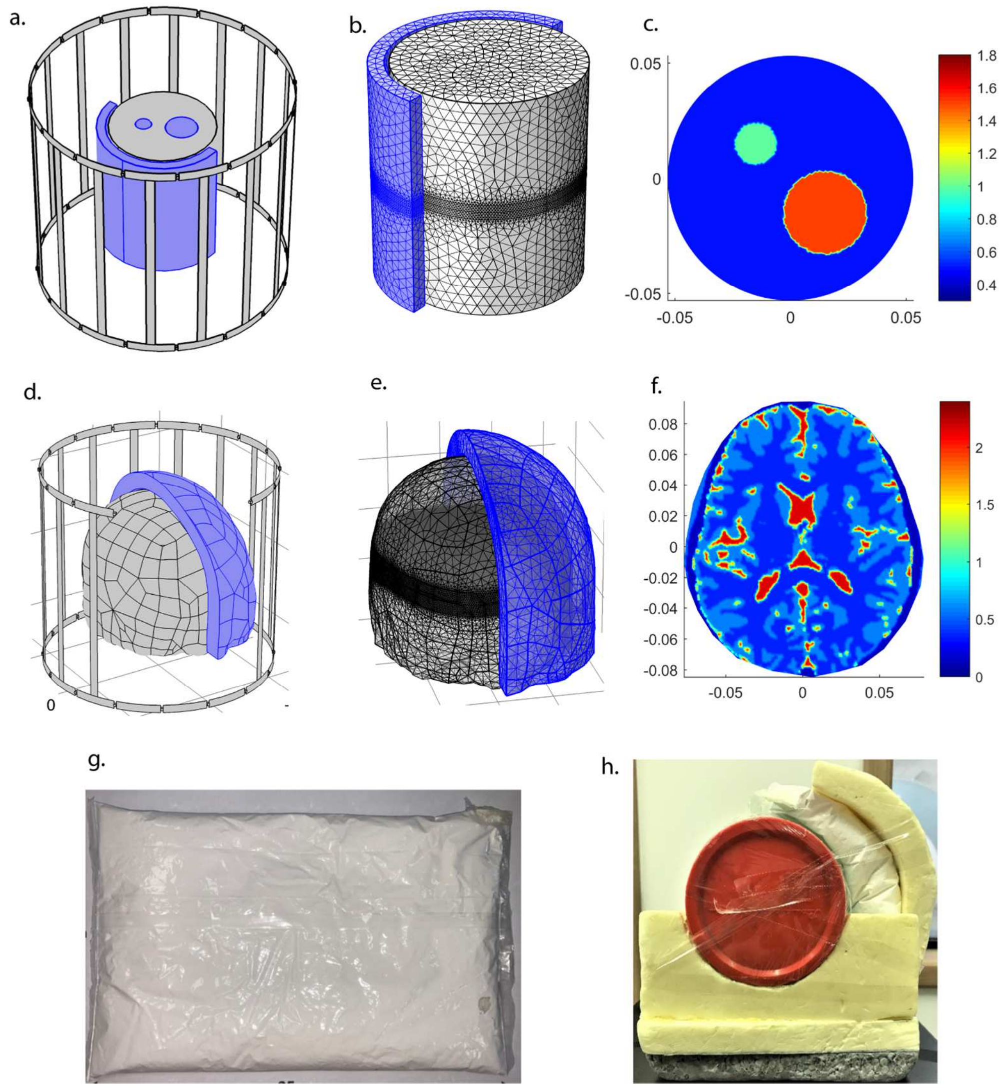

Figure 1: Simulation and experimental phantoms and pads. a) QBC, cylindrical phantom and the pad. The pad and the anomaly regions are shown with blue. b) Mesh used for the cylindrical phantom. c) Conductivity values assigned to the cylindrical phantom. d) QBC, the head phantom and the pad. e) Mesh used for the head phantom. f) Conductivity values assigned to the head phantom at the z = 0 slice. g) A $BaTiO_3$ slurry pad. h) An experimental setup with the phantom, the pad and the Styrofoam dock.

130x142mm (300 x 300 DPI)

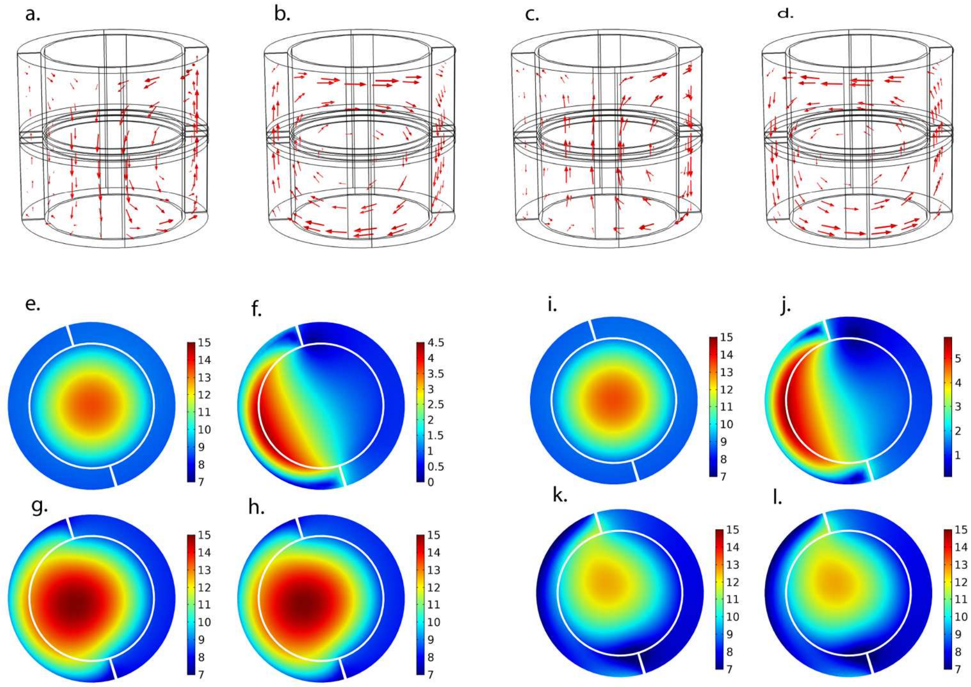

Figure 2: Effect of the pad on the H^+ magnitude and the current distribution in the pad. a-d) Current distribution in the pad (ϵ=150 ,σ=0 S/m,PT=3 cm and GT=2mm) at 0°, 90°, 180°, and 270° phase instances respectively. e-h) H_C^+, H_P^+, H_T^+, and $H_C^++H_P^+$ respectively for the same pad. i-l) H_C^+, H_P^+, H_T^+, and $H_C^++H_P^+$ respectively for another pad (ϵ=150 ,σ=2 S/m,PT=3 cm and GT=2mm).

175x123mm (300 x 300 DPI)

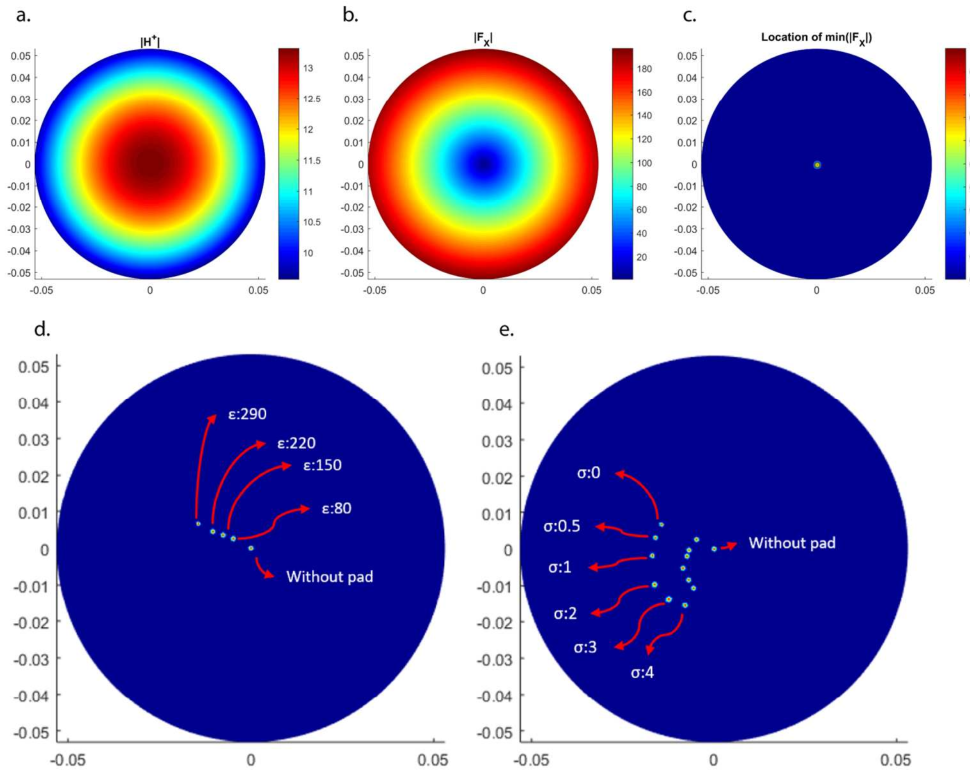

Figure 3: Effect of the EPs of the pad on the LCF shift. For homogeneous phantom without a pad, a) magnitude of H^+, b) magnitude of the convective field ($|F_X|$), and c) location of the minimum value of $|F_X|$. d) Locations of the minimum values of $|F_X|$ formed by the pads with different ϵ_r. e) Locations of the minimum values of $|F_X|$ formed by the pads with different σ (S/m); inner points are for ϵ_r=80 and the outer points are for ϵ_r=290 pads.

130x103mm (300 x 300 DPI)

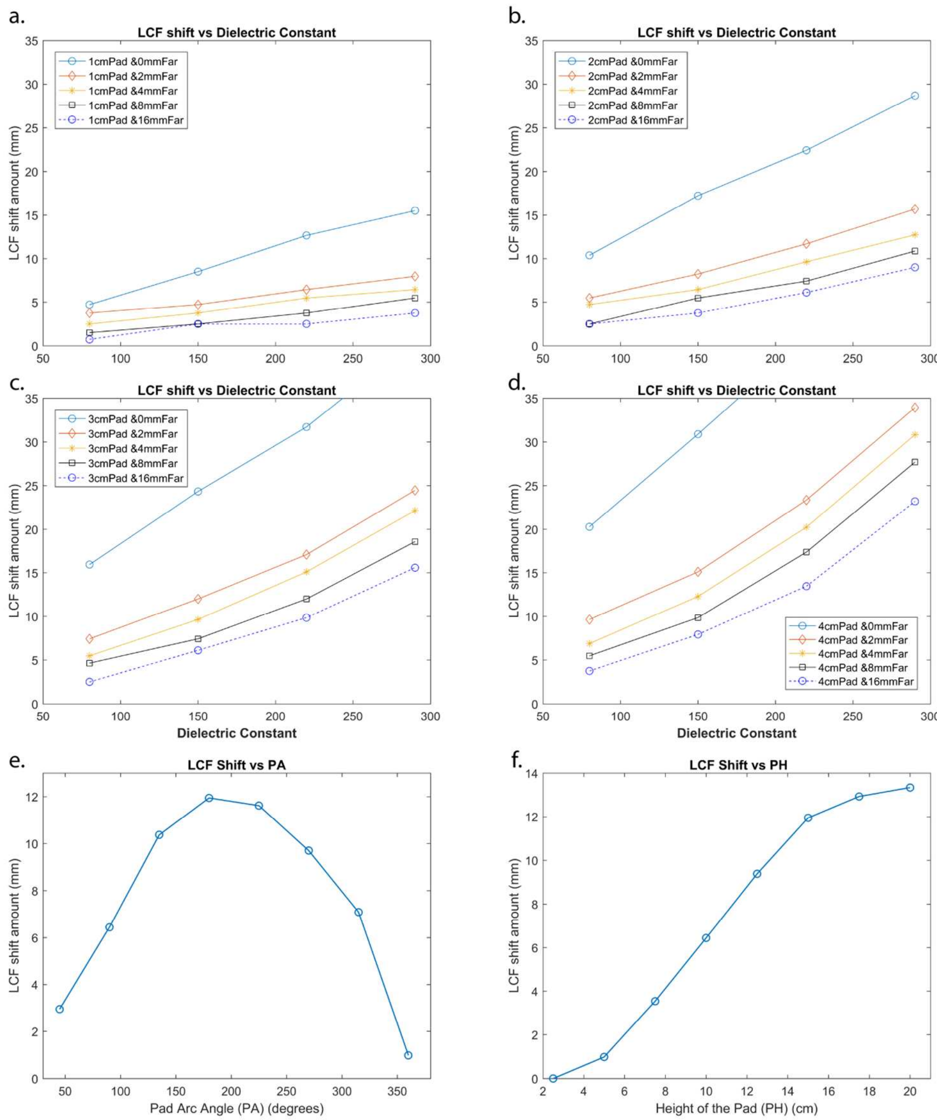

Figure 4: Effects of pad parameters on the LCF shift. LCF shift vs dielectric constant of the pad for: a) PT=1 cm, b) PT=2 cm, c) PT=3 cm, and d) PT=4 cm. Results for different GTs are shown on the same graphs. e) LCF shift vs pad angle. f) LCF shift vs pad height.

130x145mm (300 x 300 DPI)

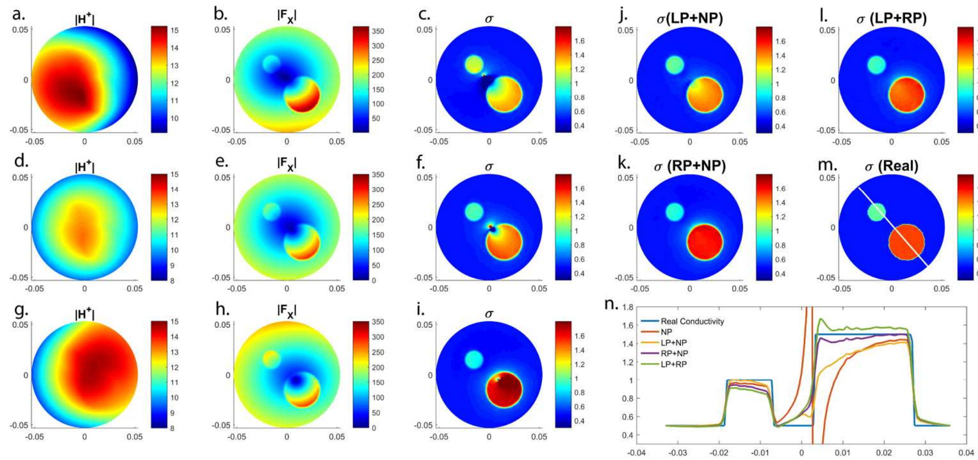

Figure 5: Simulation results with the ϵ=290 ,σ=0 S/m,PT=1 cm and GT=2mm pad. a) Magnitude of H^+. b) Magnitude of F_X. c) Reconstructed conductivity image for LP. d-f) The same images for NP. g-i) The same images for RP. j) Reconstructed conductivity image for (LP+NP) combination. k) Reconstructed conductivity image for (RP+NP) combination. l) Reconstructed conductivity image for (LP+RP) combination. m) Real conductivity map. n) Conductivity profiles on the line in m).

175x82mm (300 x 300 DPI)

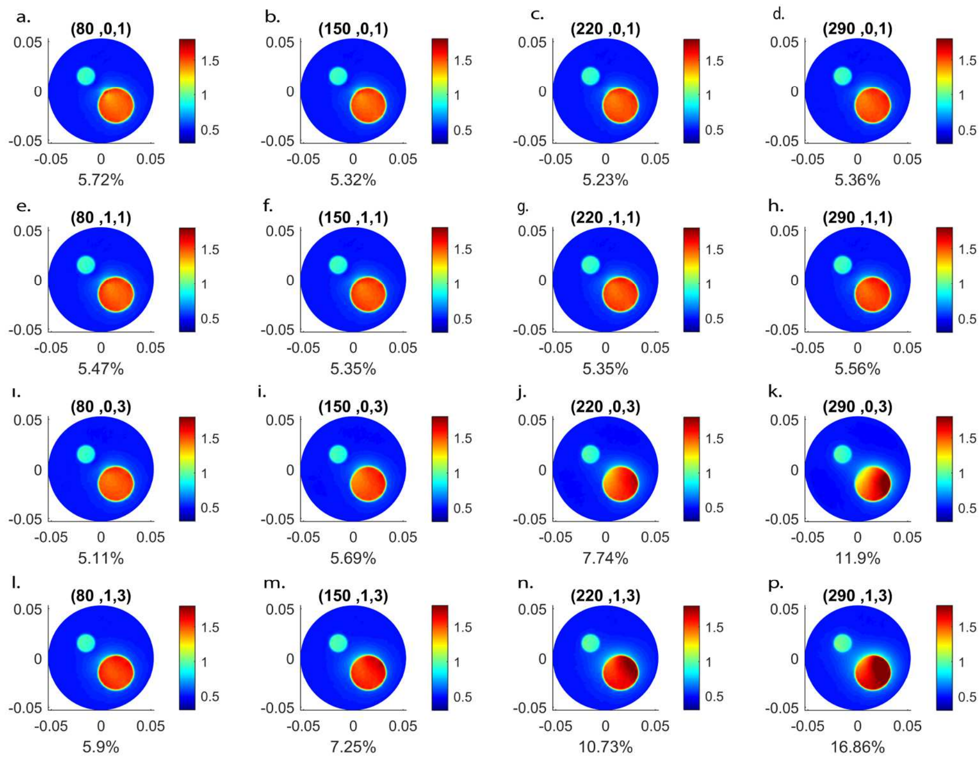

Figure 6: Reconstructed conductivity images for (LP+RP) combinations. The properties of the pad used in each simulation are indicated as (ϵ_r,σ,PT) above the figures and the corresponding percent L^2-errors are given below the figures.

175x138mm (300 x 300 DPI)

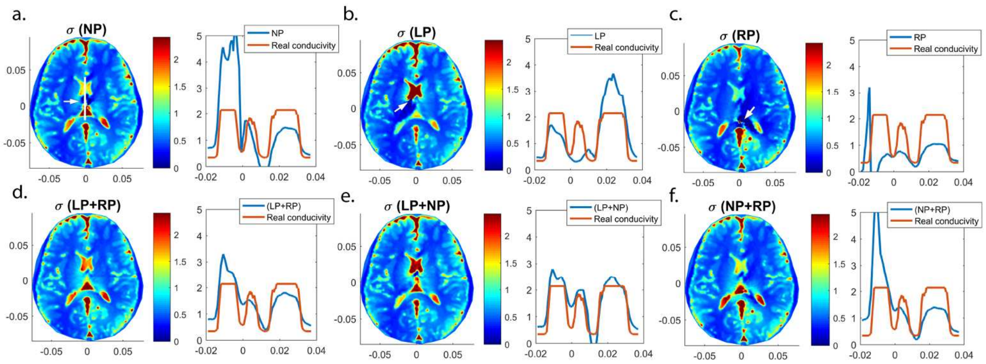

Figure 7: Head phantom simulation results. The reconstructed conductivity image for a) NP, b) LP, c) RP, d) (LP+RP), e) (LP+NP), and f) (NP+RP). For each case, conductivity profiles on the white line shown in a) are also given. LCF artifacts in a-c) are indicated with white arrows.

175x64mm (300 x 300 DPI)

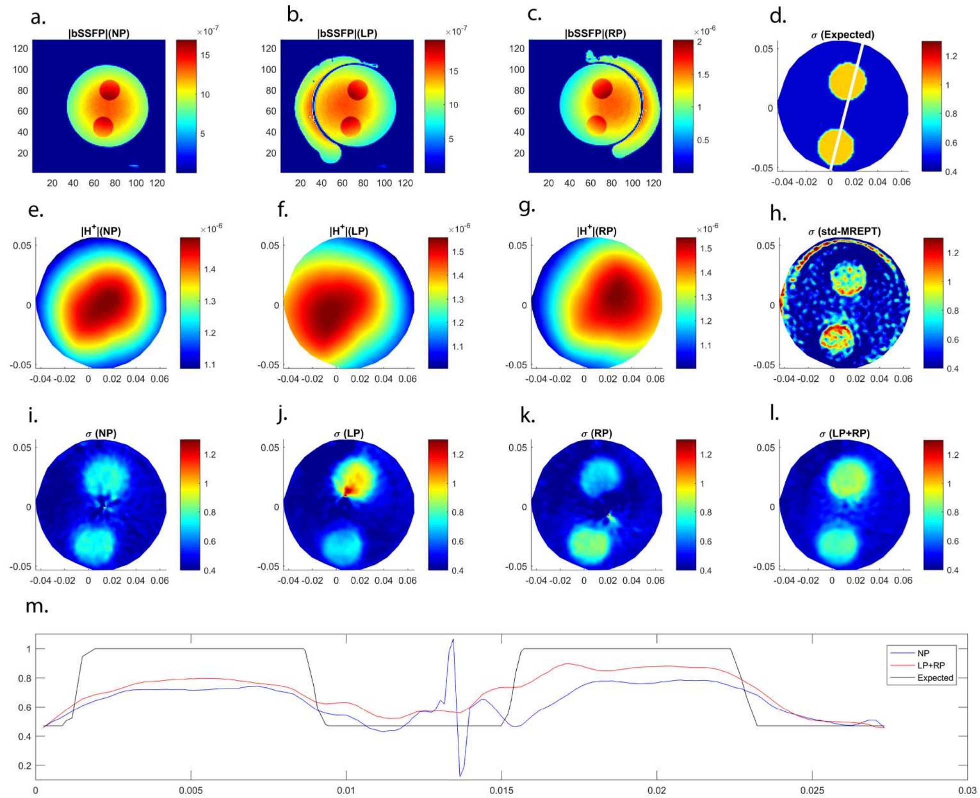

Figure 8: Experimental results with a thick water pad. bSSFP magnitude images for a) NP, b) LP, and c) RP. d) The expected conductivity map. H^+ magnitude maps for e) NP, f) LP, and g) RP. h) Conductivity image reconstructed with std-MREPT method. Reconstructed conductivity images with cr-MREPT for i) NP, j) LP, k) RP, and d) LP+RP. m) Conductivity profiles for NP and LP+RP on the line indicated in white in d).

175x142mm (300 x 300 DPI)

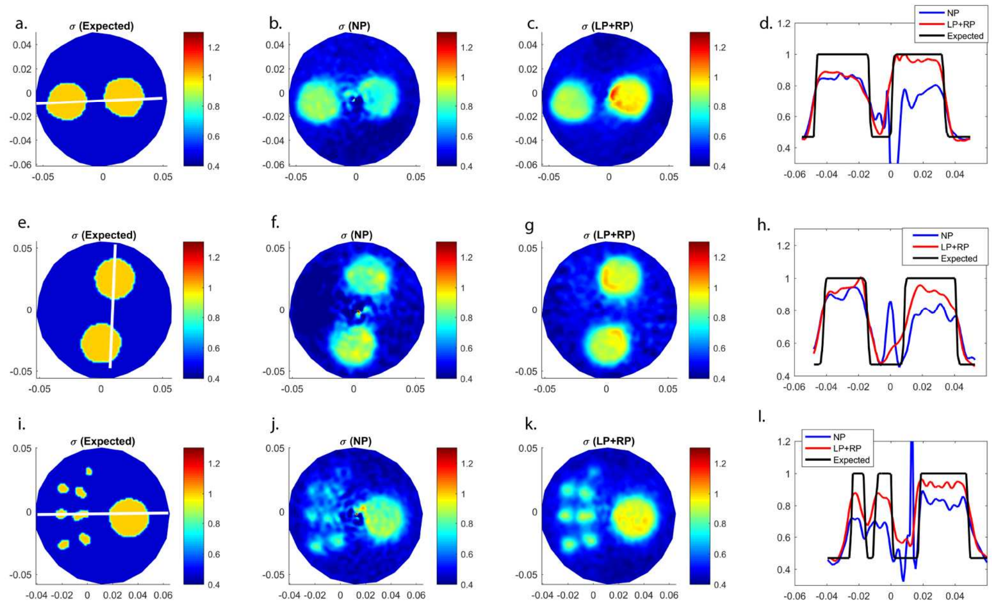

Figure 9: a-d) Results of thin water pad experiment. Expected conductivity map, reconstructed conductivity map for NP, reconstructed conductivity map for (LP+RP), and their profiles indicated with the corresponding white line respectively. e-h) Same results for non-conductive $BaTiO_3$ (Merck) pad. i-l) Same results for conductive $BaTiO_3$ (Entekno) pad.

175x109mm (300 x 300 DPI)

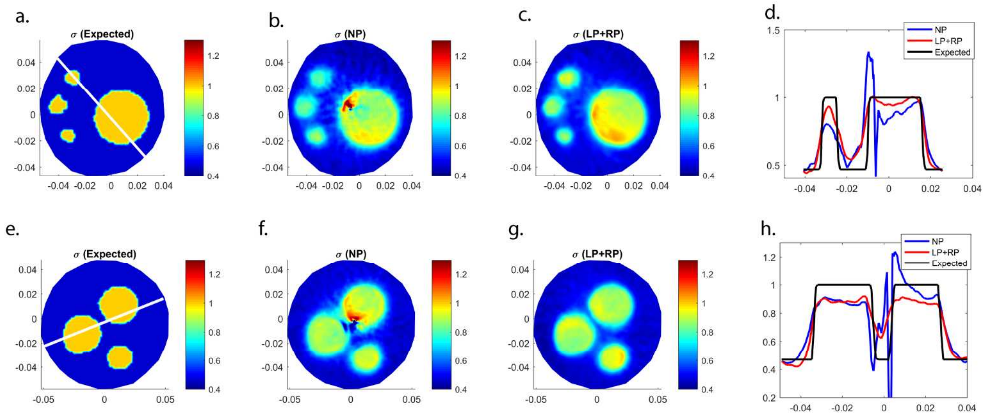

Figure 10: Experimental results with high SNR data and non-conductive $BaTiO_3$ pad. a-d) Expected conductivity map, reconstructed conductivity map for NP, reconstructed conductivity map for (LP+RP), and their profiles along the indicated white line for the 4-anomaly phantom. e-h) Same results for the 3-anomaly phantom.

175x76mm (300 x 300 DPI)